A radio pulsing white dwarf binary star

T.R. Marsh[1], B.T. Gänsicke[1], S. Hümmerich[2,3], F.-J. Hambsch[2,3,4], K. Bernhard[2,3], C.Lloyd[5], E. Breedt[1], E.R. Stanway[1], D.T. Steeghs[1], S.G. Parsons[6], O. Toloza[1], M.R. Schreiber[6], P.G. Jonker[7,8], J. van Roestel[8], T. Kupfer[9], A.F. Pala[1], V.S. Dhillon[10,11,12], L.K. Hardy[10], S.P. Littlefair[10], A. Aungwerojwit[13], S. Arjyotha[14], D. Koester[15], J.J. Bochinski[16], C.A. Haswell[16], P. Frank[2], P.J. Wheatley[1]

[1]*Department of Physics, Gibbet Hill Road, University of Warwick, Coventry, CV4 7AL, UK*
[2]*Bundesdeutsche Arbeitsgemeinschaft für Veränderliche Sterne e.V. (BAV), Berlin, Germany*
[3]*American Association of Variable Star Observers (AAVSO),Cambridge, MA, USA*
[4]*Vereniging Voor Sterrenkunde (VVS), Brugge, Belgium*
[5]*Department of Physics and Astronomy, University of Sussex, Brighton, BN1 9QH, UK*
[6]*Instituto de Física y Astronomía, Universidad de Valparaíso, Avenida Gran Bretana 1111, Valparaíso, Chile*
[7]*SRON, Netherlands Institute for Space Research, Sorbonnelaan 2, 3584-CA, Utrecht, The Netherlands*
[8]*Department of Astrophysics/IMAPP, Radboud University Nijmegen, P.O. box 9010, 6500 GL Nijmegen, The Netherlands*
[9]*Division of Physics, Mathematics and Astronomy, California Institute of Technology, Pasadena, CA 91125, USA*
[10]*Department of Physics and Astronomy, University of Sheffield, Sheffield, S3 7RH, UK*
[11]*Instituto de Astrofisica de Canarias (IAC), E-38205 La Laguna, Tenerife, Spain*
[12]*Universidad de La Laguna, Dpto. Astrofisica, E-38206 La Laguna, Tenerife, Spain*
[13]*Department of Physics, Faculty of Science, Naresuan University, Phitsanulok 65000, Thailand*
[14]*Program of Physics, Faculty of Science and Technology, Chiang Rai Rajabhat University, Chiang Rai 57100, Thailand*
[15]*Institut für Theoretische Physik und Astrophysik, University of Kiel, 24098 Kiel, Germany*
[16]*Department of Physical Sciences, The Open University, Milton Keynes, UK*

doi:10.1038/nature18620

White dwarfs are compact stars, similar in size to Earth but $\sim$ 200,000 times more massive[1]. Isolated white dwarfs emit most of their power from ultraviolet to near-infrared wavelengths, but when in close orbits with less dense stars, white dwarfs can strip material from their companions, and the resulting mass transfer can generate atomic line[2] and X-ray[3] emission, as well as near- and mid-infrared radiation if the white dwarf is magnetic[4]. However, even in binaries, white dwarfs are rarely detected at far-infrared or radio frequencies. Here we report

the discovery of a white dwarf / cool star binary that emits from X-ray to radio wavelengths. The star, AR Scorpii (henceforth AR Sco), was classified in the early 1970s as a δ-Scuti star[5], a common variety of periodic variable star. Our observations reveal instead a 3.56 hr period close binary, pulsing in brightness on a period of 1.97 min. The pulses are so intense that AR Sco's optical flux can increase by a factor of four within 30 s, and they are detectable at radio frequencies, the first such detection for any white dwarf system. They reflect the spin of a magnetic white dwarf which we find to be slowing down on a 10^7 yr timescale. The spin-down power is an order of magnitude larger than that seen in electromagnetic radiation, which, together with an absence of obvious signs of accretion, suggests that AR Sco is primarily spin-powered. Although the pulsations are driven by the white dwarf's spin, they originate in large part from the cool star. AR Sco's broad-band spectrum is characteristic of synchrotron radiation, requiring relativistic electrons. These must either originate from near the white dwarf or be generated *in situ* at the M star through direct interaction with the white dwarf's magnetosphere.

AR Sco's brightness varies on a 3.56 h period (Fig. 1a); it was this that caused the δ-Scuti classification[5]. The scatter visible in Fig. 1a prompted us to take optical photometry with the high-speed camera ULTRACAM[6]. These data and follow-up observations taken in the ultraviolet and near-infrared (Extended Data Table 1) all show strong double-humped pulsations on a fundamental period of 1.97 min (Figs 2 and 3); the scatter in Fig.1a is the result of the pulsations. Most unusually of all, an hour-long observation at radio frequencies with the Australia Telescope Compact Array (ATCA) also shows the pulsations (Figs 2d, 2e and 3d). The pulse fraction, $(f_{\rm max} - f_{\rm min})/(f_{\rm max} + f_{\rm min})$, exceeds 95 % in the far ultraviolet (Fig. 2), and is still 10 % at 9 GHz in the radio. Only in X-rays did we not detect pulses (pulse fraction < 30 % at 99.7 % confidence). AR Sco's optical magnitude (g') varies from 16.9 at its faintest to 13.6 at its peak, a factor of 20 in flux.

We acquired optical spectra which show a cool M-type main-sequence star (Extended Data Fig. 1) with absorption lines that change radial velocity sinusoidally on the 3.56 h period with amplitude $K_2 = (295 \pm 4)\,{\rm km\,s^{-1}}$ (Fig. 1b; we use subscripts "1" and "2" to indicate the compact star and the M star respectively). The 3.56 h period is therefore the orbital period of a close binary star. The M star's radial velocity amplitude sets a lower limit on the mass of its companion of $M_1 \geq (0.395 \pm 0.016)\,{\rm M}_\odot$. The compact object is not visible in the spectra, consistent with either a white dwarf or a neutron star, the only two types of object which can both support a misaligned magnetic dipole and spin fast enough to match the pulsations. The optical and ultraviolet spectra show atomic emission lines (Extended Data Figs. 1 and 2) which originate from the side of the M star facing the compact object (Extended Data Fig. 3). Their velocity amplitude relative to the M star sets a lower limit upon the mass ratio $q = M_2/M_1 > 0.35$ (Extended Data Fig. 4). This, along with the requirement that the M star fits within its Roche lobe, defines mass ranges for each star of $0.81\,{\rm M}_\odot < M_1 \lesssim 1.29\,{\rm M}_\odot$ and $0.28\,{\rm M}_\odot < M_2 \lesssim 0.45\,{\rm M}_\odot$. The

M star's spectral type (M5) suggests that its mass lies at the lower end of the allowed range for M_2. Assuming that the M star is close to its Roche lobe, its brightness leads to a distance estimate $d = (M_2/0.3\,\mathrm{M}_\odot)^{1/3}(116 \pm 16)$ pc.

The amplitude spectra of the pulsations show the presence of two components of similar frequency (Fig. 3). Using our own monitoring and archival optical data spanning 7 years[7], we measured precise values for the frequencies of these components, finding their difference to be within 20 parts per million of the orbital frequency, ν_O (Extended Data Figs 5 and 6, Extended Data Table 2). The natural interpretation is that the higher frequency component represents the spin frequency ν_S of the compact star ($P_\mathrm{S} = 1.95$ min), while its lower frequency and generally stronger counterpart is a re-processed or "beat" frequency $\nu_\mathrm{B} = \nu_\mathrm{S} - \nu_\mathrm{O}$ ($P_\mathrm{B} = 1.97$ min), assuming that the compact star spins in the same sense as the binary orbit.

AR Sco emits across the electromagnetic spectrum (Fig. 4, Extended Data Table 3), and, in the infrared and radio in particular, is orders of magnitudes brighter than the thermal emission from its component stars represented by model atmospheres[8,9] in Fig. 4. Integrating over the spectral energy distribution (SED) shown in Fig. 4 and adopting a distance of 116 pc, we find a maximum luminosity of $\approx 6.3 \times 10^{25}$ W and a mean of $\bar{L} \approx 1.7 \times 10^{25}$ W, well in excess of the combined luminosities of the stellar components $L_\star = 4.4 \times 10^{24}$ W. The two possible sources of this luminosity are accretion and spin-down power of the compact object. A spinning object of moment of inertia I loses energy at a rate $L_{\dot{\nu}} = -4\pi^2 I \nu_\mathrm{S} \dot{\nu}_\mathrm{S}$ where ν_S and $\dot{\nu}_\mathrm{S}$ are the spin frequency and its time derivative. Using the archival optical data we measured the spin frequency to be slowing, with a frequency derivative of $\dot{\nu}_\mathrm{S} = -(2.86 \pm 0.36) \times 10^{-17}\,\mathrm{Hz\,s^{-1}}$. For parameters typical of neutron stars and white dwarfs ($M_\mathrm{NS} = 1.4\,\mathrm{M}_\odot$, $R_\mathrm{NS} = 10$ km; $M_\mathrm{WD} = 0.8\,\mathrm{M}_\odot$, $R_\mathrm{WD} = 0.01\,\mathrm{R}_\odot$), this leads to $L_{\dot{\nu}}(\mathrm{NS}) = 1.1 \times 10^{21}$ W and $L_{\dot{\nu}}(\mathrm{WD}) = 1.5 \times 10^{26}$ W. Compared to the mean luminosity in excess of the stellar contributions, $L_+ = \bar{L} - L_\star = 1.3 \times 10^{25}$ W, this shows that spin-down luminosity is sufficient to power the system if the compact object is a white dwarf but not if it is a neutron star. Accretion is the only possible power source in the case of a neutron star – an accretion rate of $\dot{M}_\mathrm{NS} = 1.0 \times 10^{-14}\,\mathrm{M}_\odot\,\mathrm{yr}^{-1}$ suffices. Accretion could partially power a white dwarf, but it cannot be the main source because the rate required, $\dot{M}_\mathrm{WD} = 1.3 \times 10^{-11}\,\mathrm{M}_\odot\,\mathrm{yr}^{-1}$, is high enough that we should see Doppler-broadened emission lines from the accreting gas whereas AR Sco only shows features from the M star.

The observations point toward a white dwarf as the compact object. First, AR Sco's distance of 116 pc is an order of magnitude closer than the nearest accreting neutron star known, Cen X-4[10], but typical of white dwarf / main-sequence binaries (closer systems are known[11]). Second, AR Sco's X-ray luminosity, $L_X = 4.9 \times 10^{23}$ W, is only 4 % of the largely-optical luminosity excess, L_+. By contrast, the X-ray luminosities of accreting neutron stars are typically 100 times

their optical luminosities[12]. Third, at $P_{\rm S} = 1.95\,{\rm min}$, AR Sco has a spin period an order of magnitude longer than any (neutron star powered) radio pulsar known[13]. Finally, the upper limit masses $M_1 = 1.29\,{\rm M}_\odot$ and $M_2 = 0.45\,{\rm M}_\odot$ are simultaneously low for a neutron star but high for an M5 M star. A $0.8\,{\rm M}_\odot$ white dwarf with a $0.3\,{\rm M}_\odot$ M dwarf is a more natural pairing.

AR Sco's observational properties are unique. It may represent an evolutionary stage of a class of stars known as intermediate polars (IPs), which feature spinning magnetic white dwarfs accreting from low-mass stars in close binaries[14]. Only one IP, AE Aquarii (AE Aqr), has a broad-band SED similar to AR Sco[15] and comparably strong radio emission[16], although it shows no radio pulsations[17] ($< 0.8\,\%$) and its $0.4\,\%$ optical pulsations compare with $70\,\%$ in AR Sco. With a $25\,\%$ pulse fraction, even the IP with the strongest-known optical pulsations, FO Aquarii[18], falls well short of AR Sco. A key difference is perhaps the lack of significant accretion in AR Sco compared to the IPs. This can be seen from its X-ray luminosity which is less than $1\,\%$ of the X-ray luminosity of a typical IP[19], but above all from its optical and ultraviolet emission lines which come entirely from the irradiated face of the M star. IPs by contrast show Doppler-broadened line emission, often from accretion discs, and even AE Aqr, which is in an unusual "propeller" state in which transferred matter is expelled upon encountering the magnetosphere of its rapidly-spinning $P_{\rm S} = 33\,{\rm s}$ white dwarf[20,21], shows broad and stochastically variable line emission. We can find no analogue of AR Sco's radio properties. Pulsed radio emission has been detected from brown dwarfs and M stars[22,23], but the broad-band nature of AR Sco's emission, its short pulsation period, and lack of circular polarisation (our ATCA data constrain it to $< 10\,\%$), distinguish it from these sources.

The white dwarf in AR Sco is currently spinning down on a timescale $\tau = \nu/\dot{\nu} = 10^7\,{\rm yr}$. White dwarfs are not born spinning rapidly[24], and a prior stage of accretion-driven spin-up is required. Depending upon the distance at which the accreting material coupled to the white dwarf's magnetic field, between $0.002\,{\rm M}_\odot$ and $0.015\,{\rm M}_\odot$ of matter are required to reach $P_{\rm S} = 1.95\,{\rm min}$. For an accretion rate of $10^{-9}\,{\rm M}_\odot\,{\rm yr}^{-1}$, typical of similar period systems, this takes from $2 \times 10^7\,{\rm yr}$ to $1.5 \times 10^8\,{\rm yr}$. Both spin-up and spin-down timescales are much shorter than the likely age of the system: the cooling age of the white dwarf alone exceeds $1.2 \times 10^9\,{\rm yr}$[25]. Thus we could be seeing one of many such episodes in AR Sco's history. There is empirical evidence for similar cycling of accretion rate in both white dwarf[26,27] and neutron star binary systems[28,29]. If so, since the spin-up and spin-down timescales are similar in magnitude, there would be a good chance of catching the spin-down phase.

AR Sco's extremely broad-band SED is indicative of synchrotron emission from relativistic electrons. A significant fraction appears to come from the cool M star. We infer this from the dominant beat frequency component that in the absence of accretion can only come from the M

star. Since the M star occupies $\sim 1/40^{\rm th}$ of the sky as seen from the white dwarf, while the spin-down luminosity is ~ 11.5 times the mean electromagnetic power, this requires a mechanism to transfer energy from the white dwarf to the M dwarf which is more than $40/11.5 = 3.5$ times more efficient than the interception of isotropically-emitted radiation. At the same time, direct pulsed emission from the white dwarf must not overwhelm the re-processed component. Two possibilities are collimated fast particle outflows and direct interaction of the white dwarf's magnetosphere with the M dwarf, but the exact emission mechanism operative in AR Sco is perhaps its most mysterious feature.

References

1. Althaus, L. G., Althaus, L. G., Isern, J. & García-Berro, E. Evolutionary and pulsational properties of white dwarf stars. *Astron. & Astrophys. Review* **18,** 471–566 (2010).

2. Szkody, P. *et al.* Cataclysmic Variables from the Sloan Digital Sky Survey. VIII. The Final Year (2007-2008). *Astron. J.* **142,** 181–189 (2011).

3. Revnivtsev, M., Revnivtsev, M., Revnivtsev, M., Ritter, H. & Sunyaev, R. Properties of the Galactic population of cataclysmic variables in hard X-rays. *Astron. & Astrophys.* **489,** 1121–1127 (2008).

4. Parsons, S. G. *et al.* A magnetic white dwarf in a detached eclipsing binary. *Mon. Not. R. Astron. Soc.* **436,** 241–252 (2013).

5. Satyvaldiev, V. On seventeen variable stars. *Astronomicheskij Tsirkulyar* **633,** 7–8 (1971).

6. Dhillon, V. S. *et al.* ULTRACAM: an ultrafast, triple-beam CCD camera for high-speed astrophysics. *Mon. Not. R. Astron. Soc.* **378,** 825–840 (2007).

7. Drake, A. J. *et al.* First Results from the Catalina Real-Time Transient Survey. *Astrophys. J.* **696,** 870–884 (2009).

8. Koester, D. White dwarf spectra and atmosphere models . *Mem. della Soc. Astron. Italiana* **81,** 921–931 (2010).

9. Husser, T.-O. *et al.* A new extensive library of PHOENIX stellar atmospheres and synthetic spectra. *Astron. & Astrophys.* **553,** A6: 1–9 (2013).

10. Chevalier, C., Chevalier, C., Chevalier, C., Pedersen, H. & van der Klis, M. Optical studies of transient low-mass X-ray binaries in quiescence. I - Centaurus X-4: Orbital period, light curve, spectrum and models for the system. *Astron. & Astrophys.* **210,** 114–126 (1989).

11. Thorstensen, J. R., Lépine, S. & Shara, M. Parallax and Distance Estimates for Twelve Cataclysmic Variable Stars. *Astron. J.* **136,** 2107–2114 (2008).

12. Bradt, H. V. D. & McClintock, J. E. The optical counterparts of compact galactic X-ray sources. *Ann. Rev. Astron. & Astrophys.* **21,** 13–66 (1983).

13. Manchester, R. N., Manchester, R. N., Teoh, A. & Hobbs, M. The Australia Telescope National Facility Pulsar Catalogue. *Astron. J.* **129,** 1993–2006 (2005).

14. Patterson, J. The DQ Herculis stars. *Publ. Astron. Soc. Pacif.* **106,** 209–238 (1994).

15. Oruru, B. & Meintjes, P. J. X-ray characteristics and the spectral energy distribution of AE Aquarii. *Mon. Not. R. Astron. Soc.* **421,** 1557–1568 (2012).

16. Bookbinder, J. A. & Lamb, D. Q. Discovery of radio emission from AE Aquarii. *Astrophys. J. Lett.* **323,** L131–L135 (1987).

17. Bastian, T. S., Beasley, A. J. & Bookbinder, J. A. A Search for Radio Pulsations from AE Aquarii. *Astrophys. J.* **461,** 1016–1020 (1996).

18. Patterson, J. & Steiner, J. E. H2215-086 -King of the DQ Herculis stars. *Astrophys. J. Lett.* **264,** L61–L64 (1983).

19. Pretorius, M. L. & Mukai, K. Constraints on the space density of intermediate polars from the Swift-BAT survey. *Mon. Not. R. Astron. Soc.* **442,** 2580–2585 (2014).

20. Wynn, G. A., King, A. R. & Horne, K. A magnetic propeller in the cataclysmic variable AE Aquarii. *Mon. Not. R. Astron. Soc.* **286,** 436–446 (1997).

21. Meintjes, P. J. & Venter, L. A. The diamagnetic blob propeller in AE Aquarii and non-thermal radio to mid-infrared emission. *Mon. Not. R. Astron. Soc.* **360,** 573–582 (2005).

22. Berger, E. *et al.* Discovery of radio emission from the brown dwarf LP944-20. *Nature* **410,** 338–340 (2001).

23. Hallinan, G. *et al.* Periodic Bursts of Coherent Radio Emission from an Ultracool Dwarf. *Astrophys. J. Lett.* **663,** L25–L28 (2007).

24. Charpinet, S., Fontaine, G. & Brassard, P. Seismic evidence for the loss of stellar angular momentum before the white-dwarf stage. *Nature* **461,** 501–503 (2009).

25. Renedo, I. *et al.* New Cooling Sequences for Old White Dwarfs. *Astrophys. J.* **717,** 183–195 (2010).

26. Hessman, F. V., Gänsicke, B. T. & Mattei, J. A. The history and source of mass-transfer variations in AM Herculis. *Astron. & Astrophys.* **361,** 952–958 (2000).

27. Manser, C. J. & Gänsicke, B. T. Spectroscopy of the enigmatic short-period cataclysmic variable IR Com in an extended low state. *Mon. Not. R. Astron. Soc.* **442,** L23–L27 (2014).

28. Archibald, A. M. *et al.* A Radio Pulsar/X-ray Binary Link. *Science* **324,** 1411–1414 (2009).

29. Papitto, A. *et al.* Swings between rotation and accretion power in a binary millisecond pulsar. *Nature* **501,** 517–520 (2013).

Acknowledgements TRM, ERS, DS, EB, PJW, VSD, SPL and ULTRACAM were supported by the Science and Technology Facilities Council (STFC, ST/L000733 and ST/M001350/1). BTG, AP and PGJ acknowledge support from the European Research Council (ERC, 320964 and 647208). OT, SGP and MRS acknowledge support from Fondecyt (3140585 and 1141269). MRS also received support from Millenium Nucleus RC130007 (Chilean Ministry of Economy). AA acknowledges support from the Thailand Research Fund (MRG5680152) and the National Research Council of Thailand (R2559B034). Based on observations collected with telescopes of the Isaac Newton Group in the Spanish Observatorio del Roque de los Muchachos of the Instituto de Astrofísica de Canarias, the European Organisation for Astronomical Research in the Southern Hemisphere (095.D-0489, 095.D-0739, 095.D-0802), the NASA/ESA Hubble Space Telescope (14470), and the Thai National Telescope. Archival data from the *Herschel*, *Spitzer* and WISE space observatories, and from the Catalina Sky Survey were used. We thank the *Swift* mission PI for a target-of-opportunity program on AR Sco with the XRT and UVOT instruments, and the Director of ATCA for the award of Director's Discretionary Time.

Competing Interests The authors declare that they have no competing financial interests.

Author contributions TRM organised observations, analysed the data, interpreted the results and was the primary author of the manuscript. BTG, AFP, EB, SGP, PGJ, JvR, TK, MRS, and OT acquired, reduced and analysed optical and ultraviolet spectroscopy. ERS acquired, reduced and analysed the ATCA radio data. SH, FJH, KB, CL and PF first identified the unusual nature of AR Sco and started the optical monitoring campaign. VSD, LKH, SPL, AA, SA, JJB and CAH acquired and reduced the high-speed optical photometry. DTS and PJW acquired and analysed *Swift* and archival X-ray data. DK calculated the white dwarf model atmosphere. All authors commented on the manuscript.

Correspondence Correspondence and requests for materials should be addressed to TRM.
(email: t.r.marsh@warwick.ac.uk).

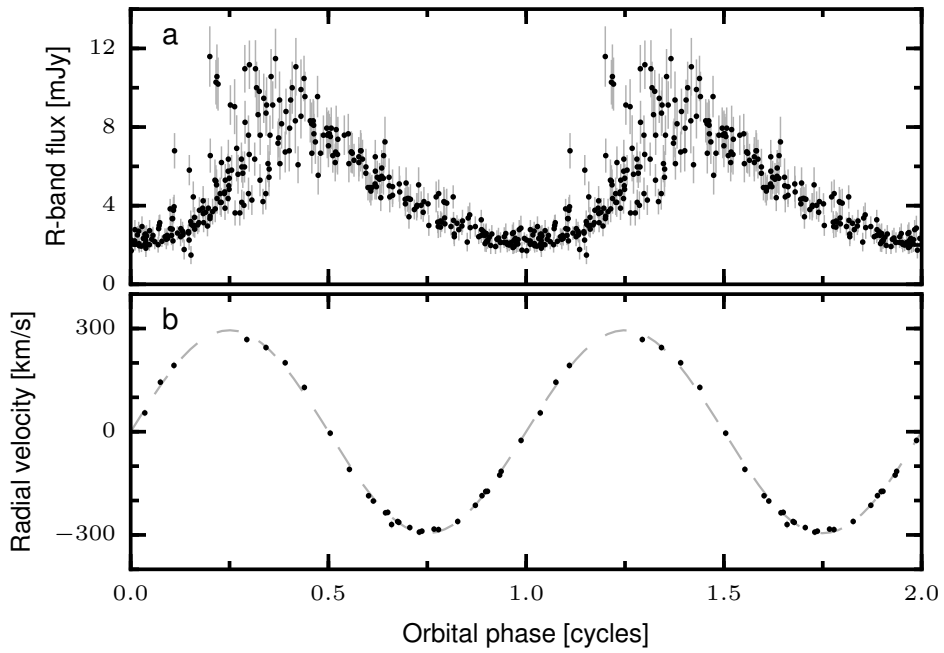

Figure 1: AR Sco's optical brightness and radial velocity curve. a, Photometry ($30\,\mathrm{s}$ exposures) taken over 7 years shows a factor four variation in brightness on a $3.56\,\mathrm{h}$ period, with large scatter at some phases. **b**, The M star varies sinusoidally in velocity on the same period, showing it to be the orbital period of a close, circular orbit binary star. The orbital phase is defined so that at phase 0 the M star is at its closest point to Earth. $\pm 1\sigma$ error bars are shown, but are too small to see in **b**.

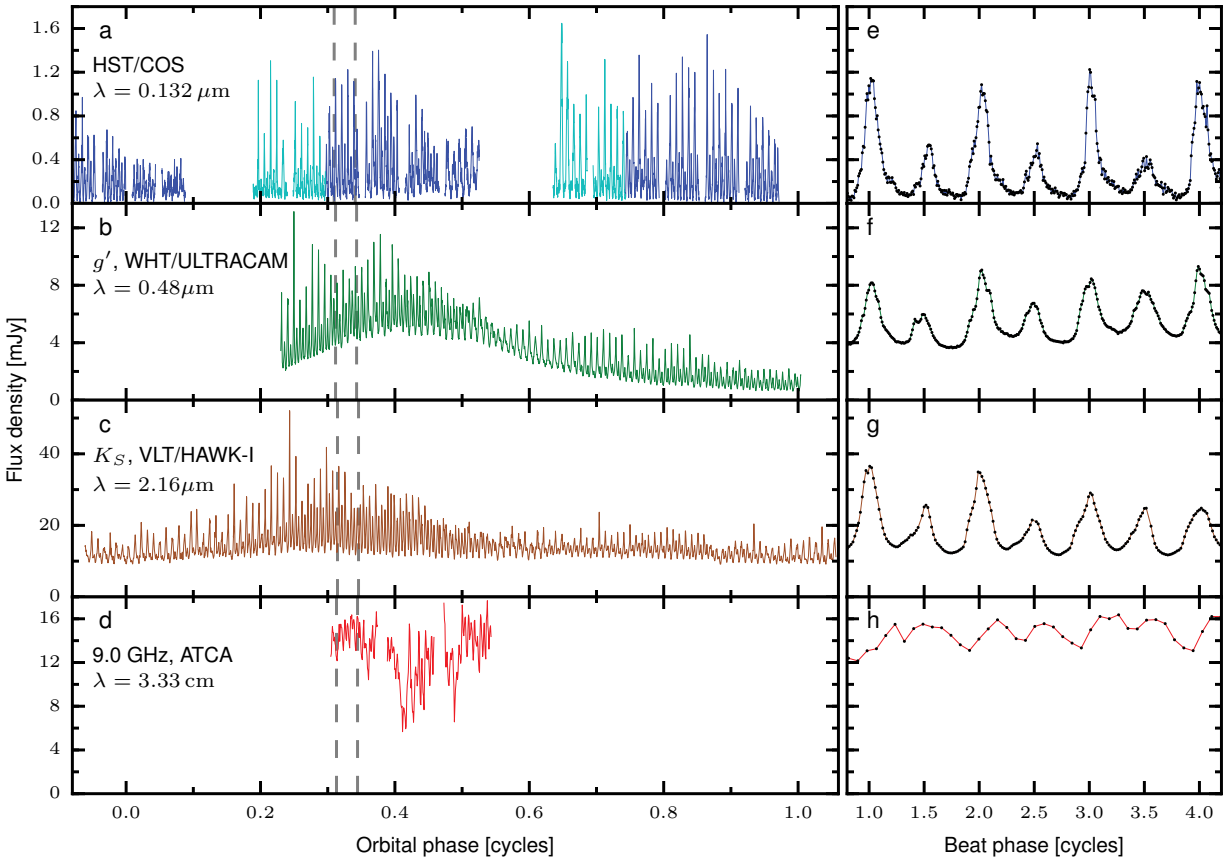

Figure 2: Ultraviolet, optical, infrared and radio fluxes of AR Sco. a–d, High-speed measurements of the UV, optical, infrared and radio fluxes of AR Sco plotted against orbital phase. Sections of similar orbital phases, marked by dashed lines, are shown expanded in **e–h** where they are plotted against the beat pulsation phase. Black dots mark individual measurements. None of the four sets of data were taken simultaneously in time. The different colours in **a** indicate that the data were acquired in different orbital cycles.

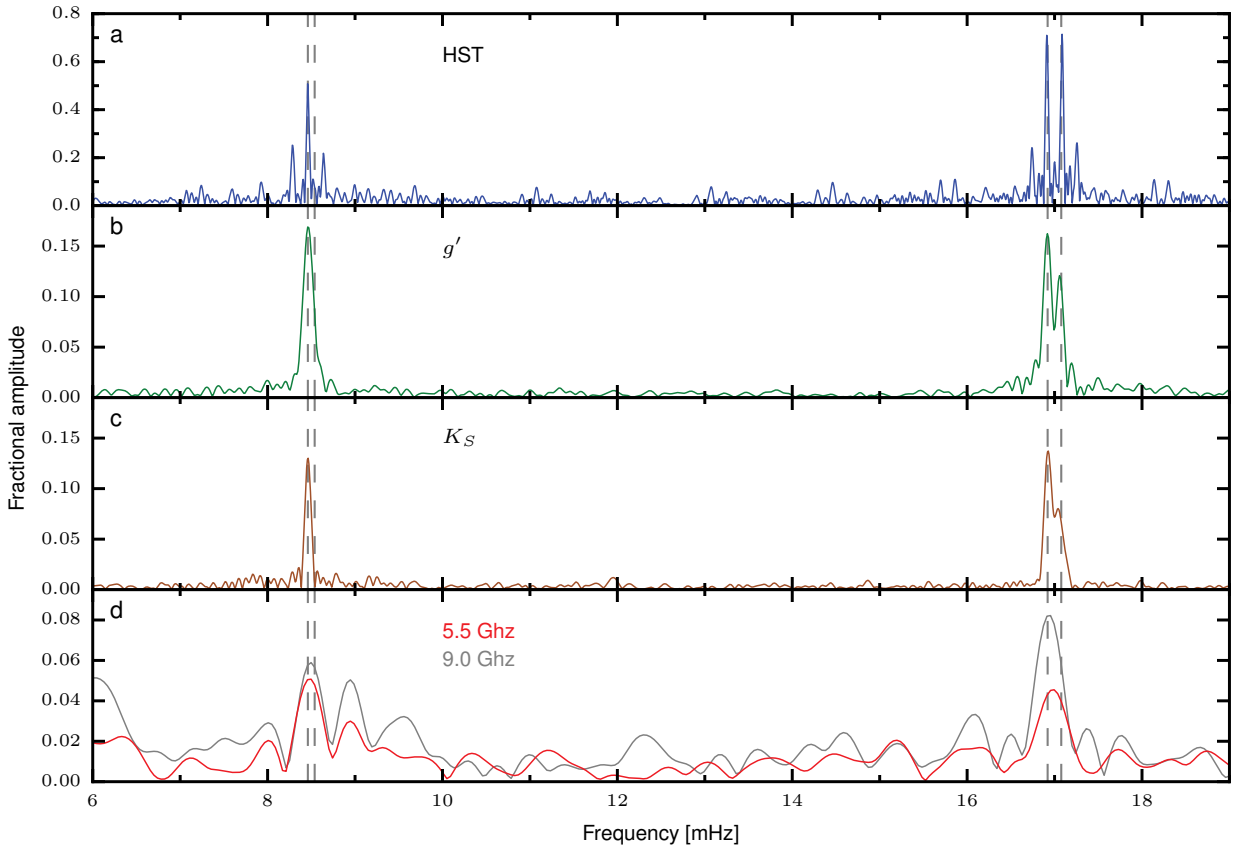

Figure 3: Fourier amplitudes of the ultraviolet, optical, infrared and radio fluxes of AR Sco versus temporal frequency . a–d are the amplitude spectra corresponding to **a–d** of the light-curves of Fig. 2. All bands show signals with a fundamental period of $\sim 1.97\,\mathrm{min}$ $(8.46\,\mathrm{mHz})$ and its second harmonic. The signals have two components, clearest in the harmonic, which we identify as the spin frequency ν_S and "beat" frequency $\nu_\mathrm{B} = \nu_\mathrm{S} - \nu_\mathrm{O}$, where ν_O is the orbital frequency. The beat component is the stronger of the two and defines the dominant $1.97\,\mathrm{min}$ pulsation period; the spin period is $1.95\,\mathrm{min}$.

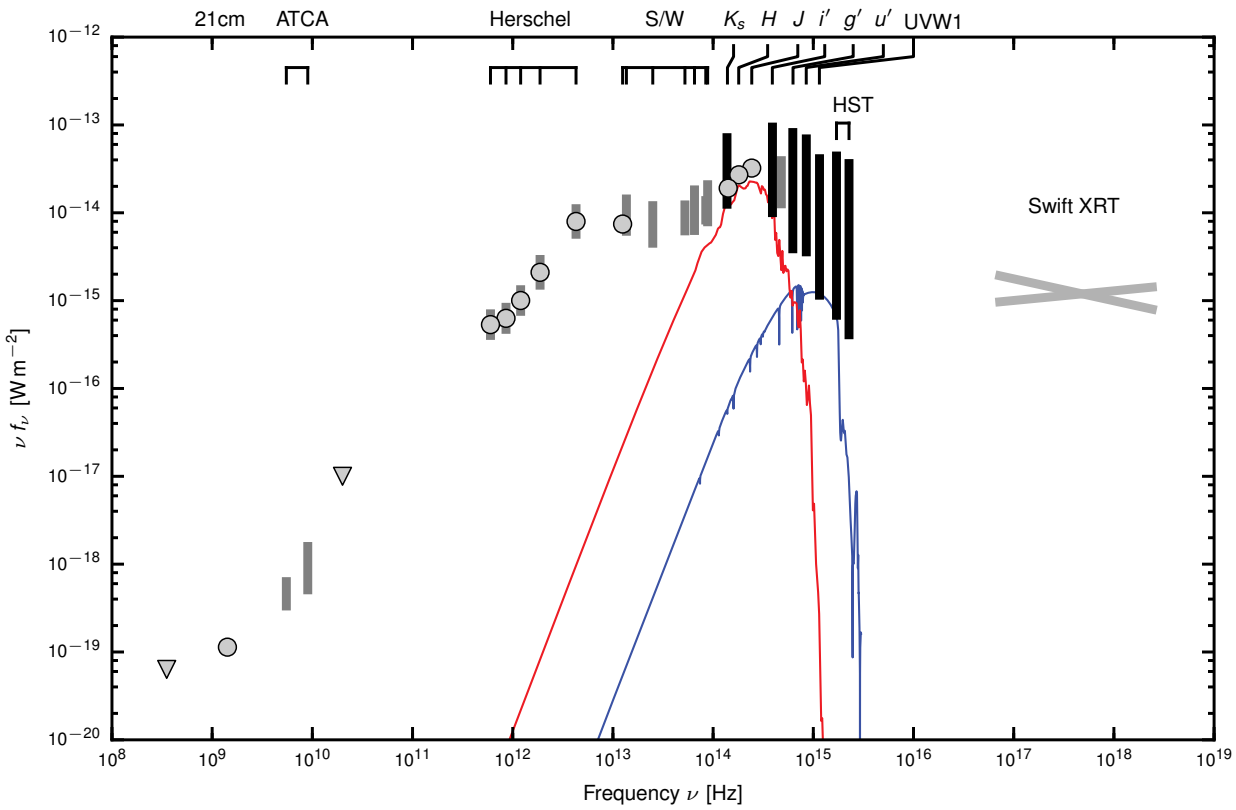

Figure 4: The wide band Spectral Energy Distribution (SED) of AR Sco. Black bars show the range spanned by intensive, time-resolved data; grey bars represent more limited datasets spanning less than the full variation. Grey points with error bars (1σ) represent single exposures. The grey lines represent the $\pm 1\sigma$ range of X-ray spectral slopes. Triangles are upper-limits. "S/W" marks data from *Spitzer* and WISE. The red and blue lines show model atmospheres, extended at long wavelengths with black-body spectra, for the M star ($R_2 = 0.36\,\mathrm{R}_\odot$, $T_2 = 3100\,\mathrm{K}$) and white dwarf ($R_1 = 0.01\,\mathrm{R}_\odot$, $T_2 = 9750\,\mathrm{K}$ upper limit) at a distance $d = 116\,\mathrm{pc}$. See Extended Data Tables 1 and 3 for details of data sources.

Methods

Data sources. AR Sco's location in the ecliptic plane, not far from the Galactic centre and only 2.5° North-West of the centre of the Ophiuchus molecular cloud, means that it appears in many archival observations. It is detected in the FIRST 21 cm radio survey[30], the Two Micron All Sky Survey (2MASS)[31], the Catalina Sky Survey (CSS)[7], and in the *Herschel*, WISE and *Spitzer* infrared satellite archives[32,33,34]. Useful upper limits come from non-detections in the Australia Telescope 20 GHz (AT20G) survey[35] and the WISH survey[36]. Flux measurements, ranges (when time resolved data are available) and upper limits from these sources are listed in Extended Data Table 3.

We supplemented these data with our own intensive observations on a variety of telescopes and instruments, namely: the 8.2 m Very Large Telescope (VLT) with the FORS and X-SHOOTER optical/NIR spectrographs and the HAWK-I NIR imager; the 4.2 m William Herschel Telescope (WHT) with the ISIS spectrograph and the ULTRACAM high-speed camera[6]; the 2.5 m Isaac Newton Telescope (INT) with the Intermediate Dispersion Spectrograph (IDS); the 2.4 m Thai National Telescope with the ULTRASPEC high-speed camera[37]; the UV/optical and X-ray instruments UVOT and XRT on the *Swift* satellite; the COS UV spectrograph on the Hubble Space Telescope, *HST*; radio observations on the Australia Telescope Compact Array (ATCA). Optical monitoring data came from a number of small telescopes. We include here data taken with a 406 mm telescope at the Remote Observatory Atacama Desert (ROAD) in San Pedro de Atacama[38]. Extended Data Table 1 summarises these observations.

The orbital, spin and beat frequencies. The orbital, spin and beat frequencies were best measured from the small-telescope data because of their large time-base. For example, see the amplitude spectrum around the spin/beat components of the clear filter data from 19–28 July 2015 shown in Extended Data Fig. 5. The final frequencies, which give the dashed lines of Extended Data Fig. 5, were obtained from the CSS data. These consisted of 305 exposures each 30-seconds in duration spanning the interval 30 May 2006 until 8 July 2013. We rejected 6 points which lay more than 4σ from the multi-sinusoid fits that we now describe. To search for signals in these sparsely-sampled data, we first transformed the UTC times of the CSS data to a uniform timescale (TDB) and then corrected these for light-travel delays to the solar system barycentre. The periodogram of these data is dominated by the strong orbital modulation, which leaks so much power across the spectrum owing to the sparse sampling that the spin/beat component can only be seen after the orbital signal is removed. Once this was done, beat and spin components matching those of Extended Data Fig. 5 could be identified (Extended Data Fig. 6). We carried out bootstrap multi-sinusoid fits to compute the distributions of the orbital, beat and spin frequencies. The orbital frequency closely follows a Gaussian distribution; the beat and spin distributions are somewhat non-Gaussian in their high and low frequency wings respectively, but are nevertheless well-defined. Statistics computed

from these distributions are listed in Extended Data Table 2.

Having established that the two pulsation frequencies are separated by the orbital frequency, we carried out a final set of fits in which we enforced the relation $\nu_{\rm S} - \nu_{\rm B} = \nu_{\rm O}$, but also allowed for a linear drift of the pulsation frequency in order to be sensitive to any change in the pulsation frequency. This led to a significant improvement in χ^2 ($> 99.99\%$ significance on an F-test) which dropped from 326 to 289 for the 299 fitted points relative to a model in which the frequencies did not vary (after scaling uncertainties to yield $\chi^2/N \approx 1$ for the final fit). Bootstrap fits gave a near-Gaussian distribution for the frequency derivative with $\dot{\nu} = -(2.86 \pm 0.36) \times 10^{-17}\,{\rm Hz\,s^{-1}}$.

Pulsations are detected at all wavelengths with suitable data other than X-rays, where limited signal (≈ 630 source photons in 10.2 ks) leads to the upper limit of a 30 % pulse fraction quoted in the main text. The *Swift* X-ray observations were taken in 1000 s chunks over the course of more than one month and we searched for the pulsations by folding into 20 bins and fitting a sinusoid to the result. There were no significant signals on either the beat or spin periods or their harmonics. We used a power-law fit to the X-ray spectrum to deduce the slopes shown in Fig. 4.

The M star's spectral type and distance. The CSS data establish the orbital period $P = 0.14853528(8)$ d, but not the absolute phase of the binary. This we derived from observations of the M star, which also led to a useful constraint upon the distance to the system. The VLT+FORS data were taken shortly before the photometric minimum, allowing a clear view of the M star's contribution. We used M star spectral-type templates developed from SDSS spectra[39] to fit AR Sco's spectrum, applying a flux scaling factor α to the selected template and adding a smooth continuum to represent any extra flux in addition to the M star. The smooth spectrum was parameterised by $\exp(a_1 + a_2\lambda)$ to ensure positivity. The coefficients a_1, a_2 and α were optimised for each template, with emission lines masked since they are not modelled by the smooth spectrum. Out of the templates available (M0-9 in unit steps), the M5 spectrum gave by far the best match with $\chi^2 = 24{,}029$ for 1165 points fitted compared to $> 100{,}000$ for the M4 and M6 templates on either side (Extended Data Fig. 1). The templates used were normalised such that the scaling factor $\alpha = (R_2/d)^2$. We found $\alpha = 3.02 \times 10^{-21}$, so $R_2/d = 5.5 \times 10^{-11}$. Assuming that the M star is close to its Roche lobe (there is evidence supporting this assumption in the form of ellipsoidal modulations of the minima between pulsations in the HAWK-I data, Fig. 2), its mean density is fixed by the orbital period, which means that its radius is fixed by its mass. Assuming $M_2 = 0.3\,{\rm M}_\odot$, for reasons outlined in the main text, we find that $R_2 = 0.36\,{\rm R}_\odot$, and hence $d = 149$ pc. This is an overestimate as the FORS spectrum was taken through a narrow slit. We estimated a correction factor by calculating the i'-band flux of the spectrum (2.50 mJy) and comparing it to the mean i'-band flux (4.11 mJy) of the ULTRACAM photometry over the same range of orbital phase. This is approximate given that the ULTRACAM data were not taken simultaneously with the FORS data and there may be stochastic variations in brightness from orbit-to-orbit, however the implied 61 % throughput is

plausible given the slit width of 0.7" and seeing of ~ 1". The final result is the distance quoted in the main text of $d = (116 \pm 16)$ pc, and allows for uncertainties in the calibration of the surface brightness of the templates and in the slit-loss correction.

We used the radius, spectral type and distance to estimate the K_S flux density from the donor as $f_{Ks} = 9.4$ mJy. The minimum observed flux density from the HAWK-I data is 9.1 mJy. Uncertainties in the extrapolation required to estimate the K_S flux and from ellipsoidal modulations allow the numbers to be compatible, but they suggest that the estimated distance is as low as it can be and that the M star dominates the K_S flux at minimum light. The estimated M star fluxes for i' and g', $f_{i'} = 1.79$ mJy and $f_{g'} = 0.07$ mJy, are comfortably less than the minimum observed fluxes of 2.57 mJy and 0.624 mJy in the same bands. We do not detect the white dwarf. The strongest constraint comes from the *HST* far ultraviolet data which at its lowest require $T_1 < 9750$ K. A white dwarf model atmosphere of $T = 9750$ K, $\log g = 8$, corrected for slit-losses is plotted in Fig. 1, and also (without slit losses) in Fig. 2 which shows the average *HST* spectrum. Given the small maximum contribution of the white dwarf seen in these figures, the absence of absorption features from the white dwarf is unsurprising.

The M star's radial velocity. We used spectra taken with the ISIS spectrograph on the WHT and X-SHOOTER on the VLT to measure radial velocities of the M star using the NaI 8200 doublet lines. These vary sinusoidally on the same 3.56 h period as the slowest photometric variation (Fig. 1), hence our identification of this period as the orbital period. We fitted the velocities with

$$V_R = \gamma + K_2 \sin\left(2\pi(t - T_0)/P\right),$$

with the period fixed at the value obtained from the CSS data, $P = 0.14853528$ d, and the systemic offset γ allowed to float free for each distinct subset of the data to allow for variable offsets. We found $K_2 = (295 \pm 4)$ km s^{-1} and $T_0 = 57264.09615(33)$ d, thus the orbital ephemeris of AR Sco is

$$\mathrm{BMJD(TDB)} = 57264.09615(33) + 0.14853528(8)E,$$

where E is the cycle number, and the time scale is TDB, corrected to the barycentre of the solar system, expressed as a Modified Julian Day number ($\mathrm{MJD} = \mathrm{JD} - 2400000.5$). This ephemeris is important in establishing the origin of the emission lines, as will be shown below.

The radial velocity amplitude and orbital period along with Kepler's third law define the "mass function"

$$\frac{M_1^3 \sin^3 i}{(M_1 + M_2)^2} = \frac{P K_2^3}{2\pi G} = (0.395 \pm 0.016)\,\mathrm{M}_\odot,$$

where i is the orbital inclination. This is a hard lower limit to the mass of the compact object, M_1, which is only met for $i = 90°$ and $M_2 = 0$. There is however a caveat to this statement: it is sometimes observed that irradiation can weaken the absorption lines on the side of the cool star

facing the compact object causing the observed radial velocity amplitude to be an over-estimate of the true amplitude[40,41]. If this effect applied here, which we suspect it might, both K and the mass function limit would need to be reduced. Given the large intrinsic variability of AR Sco, and the lack of flux-calibrated spectra, it was not possible to measure the absolute strength of NaI. We attempted therefore to search for the influence of irradiation from another side effect, which is that it causes the radial velocity to vary non-sinusoidally[42]. We failed to detect any obvious influence of irradiation through this method, but its effectiveness may be limited by the heterogeneous nature of our data which required multiple systematic velocity offsets. Despite our failure to detect clear signs of the effect of irradiation upon the M star's radial velocities, we would not be surprised if the true value of K was anything up to $\sim 20\,\mathrm{km\,s^{-1}}$ lower than we measure. However, with no clear evidence for the effect, in this we paper we proceed on the basis that we have measured the true value of the M star's centre of mass radial velocity amplitude. This is conservative in the sense that any reduction in K would move the mass limits we deduce to lower values, which would tilt the balance even more heavily towards a white dwarf as the compact star. The UV and optical emission lines come from the irradiated face of the M star and their amplitude compared to K_2 sets a lower limit to the relative size of the M star, and hence, through Roche geometry, the mass ratio $q = M_2/M_1$. Extended Data Fig. 4 shows how the emission measurements lead to the quoted limit of $q > 0.35$, which leads in turn to the lower limits $M_1 > 0.81\,\mathrm{M}_\odot$ and $M_2 > 0.28\,\mathrm{M}_\odot$ quoted in the main text.

The orbital period of a binary star sets a lower limit on the mean densities of its component stars[43]. Since the mean densities of main-sequence stars decrease with increasing mass, this implies that we can set an upper limit to the mass of any main-sequence component. In the case of AR Sco we find that $\langle\rho_2\rangle > 8900\,\mathrm{kg\,m^{-3}}$ which leads to $M_2 < 0.42\,\mathrm{M}_\odot$; the slightly larger value of $0.45\,\mathrm{M}_\odot$ quoted in the text allows for uncertainty in the models. The limit becomes an equality when the M star fills its Roche lobe, which we believe to be the case, or very nearly so, for AR Sco. However, we expect that even in this case the number deduced still functions as an upper limit because the mass-losing stars in close binaries are generally over-sized and therefore less dense than main-sequence stars of the same mass[44]. Indeed, systems with similar orbital periods to that of AR Sco have donor star masses in the range $0.2\,\mathrm{M}_\odot$ to $0.3\,\mathrm{M}_\odot$[44]. This, and the M5 spectral type, are why we favour a mass of $M_2 \approx 0.3\,\mathrm{M}_\odot$, close to the lower limit on M_2.

Brightness temperature at radio wavelengths. The pulsations in radio flux are a remarkable feature of AR Sco, unique amongst known white dwarfs and white dwarf binaries. If we assume that, as at other wavelengths, and as suggested by the alignment of the second harmonic power with $2\nu_\mathrm{B}$ (Extended Data Fig. 3), they arise largely from the M star, then we can deduce brightness temperatures from the relation

$$T_b = \frac{\lambda^2}{2\pi k}\left(\frac{d}{R_2}\right)^2 f_\nu.$$

These work out to be $\approx 10^{12}$ K and $\approx 10^{13}$ K for the observations at $\nu = 5.5$ GHz and $\nu = 1.4$ GHz respectively. Although the value at the lowest frequency exceeds the $\sim 10^{12}$ K limit at which severe cooling of the electrons due to inverse Compton scattering is thought to occur[45], this is not necessarily a serious issue given the short-term variability exhibited by the source. The limits can be lowered by appealing to a larger emission region as the radio data in hand are not enough to be certain that emission arises solely on the M star. Even so, the 0.98 min second harmonic pulsations that are seen in the radio flux suggest an upper limit to the size of the emission region of $25\,\mathrm{R}_\odot$ from light-travel time alone. This implies a minimum brightness temperature of 10^9 K at 1.4 GHz, showing clearly that the radio emission is non-thermal in origin. We assume that synchrotron emission dominates; while there may be thermal and cyclotron components at shorter wavelengths, there is no clear evidence for either.

Code availability. The data were reduced with standard instruments pipelines for the *HST*, VLT, and *Swift* data. The WHT and INT data were reduced with STARLINK software. Scripts for creating the figures are available from the first author apart from the code for computing the white dwarf model atmosphere, which is a legacy F77 code and complex to export. The atmosphere model itself however is available on request.

30. Becker, R. H., White, R. L. & Helfand, D. J. The FIRST Survey: Faint Images of the Radio Sky at Twenty Centimeters. *Astrophys. J.* **450,** 559–577 (1995).

31. Skrutskie, M. F. *et al.* The Two Micron All Sky Survey (2MASS). *Astron. J.* **131,** 1163–1183 (2006).

32. Pilbratt, G. L. *et al.* Herschel Space Observatory. An ESA facility for far-infrared and submillimetre astronomy. *Astron. & Astrophys.* **518,** L1–L6 (2010).

33. Wright, E. L. *et al.* The Wide-field Infrared Survey Explorer (WISE): Mission Description and Initial On-orbit Performance. *Astron. J.* **140,** 1868–1881 (2010).

34. Werner, M. W. *et al.* The Spitzer Space Telescope Mission. *Astrophys. J. Supp.* **154,** 1–9 (2004).

35. Murphy, T. *et al.* The Australia Telescope 20 GHz Survey: the source catalogue. *Mon. Not. R. Astron. Soc.* **402,** 2403–2423 (2010).

36. De Breuck, C., De Breuck, C., De Breuck, C., Röttgering, H. & van Breugel, W. A sample of ultra steep spectrum sources selected from the Westerbork In the Southern Hemisphere (WISH) survey. *Astron. & Astrophys.* **394,** 59–69 (2002).

37. Dhillon, V. S. *et al.* ULTRASPEC: a high-speed imaging photometer on the 2.4-m Thai National Telescope. *Mon. Not. R. Astron. Soc.* **444,** 4009–4021 (2014).

38. Hambsch, F.-J. ROAD (Remote Observatory Atacama Desert): Intensive Observations of Variable Stars. *Journal of the American Association of Variable Star Observers (JAAVSO)* **40,** 1003–1009 (2012).

39. Rebassa-Mansergas, A., Rebassa-Mansergas, A., Rebassa-Mansergas, A., Schreiber, M. R. & Koester, D. Post-common-envelope binaries from SDSS - I. 101 white dwarf main-sequence binaries with multiple Sloan Digital Sky Survey spectroscopy. *Mon. Not. R. Astron. Soc.* **382,** 1377–1393 (2007).

40. Hessman, F. V., Hessman, F. V., Nather, R. E. & Zhang, E.-H. Time-resolved spectroscopy of SS Cygni at minimum and maximum light. *Astrophys. J.* **286,** 747–759 (1984).

41. Wade, R. A. & Horne, K. The radial velocity curve and peculiar TiO distribution of the red secondary star in Z Chamaeleontis. *Astrophys. J.* **324,** 411–430 (1988).

42. Marsh, T. R. A spectroscopic study of the deeply eclipsing dwarf nova IP Peg. *Mon. Not. R. Astron. Soc.* **231,** 1117–1138 (1988).

43. Faulkner, J., Flannery, B. P. & Warner, B. Ultrashort-Period Binaries. II. HZ 29 (=AM CVn): a Double-White Semidetached Postcataclysmic Nova?. *Astrophys. J. Lett.* **175,** L79–L83 (1972).

44. Knigge, C., Baraffe, I. & Patterson, J. The Evolution of Cataclysmic Variables as Revealed by Their Donor Stars. *Astrophys. J. Supp.* **194,** 28–75 (2011).

45. Kellermann, K. I. & Pauliny-Toth, I. I. K. The Spectra of Opaque Radio Sources. *Astrophys. J. Lett.* **155,** L71–L78 (1969).

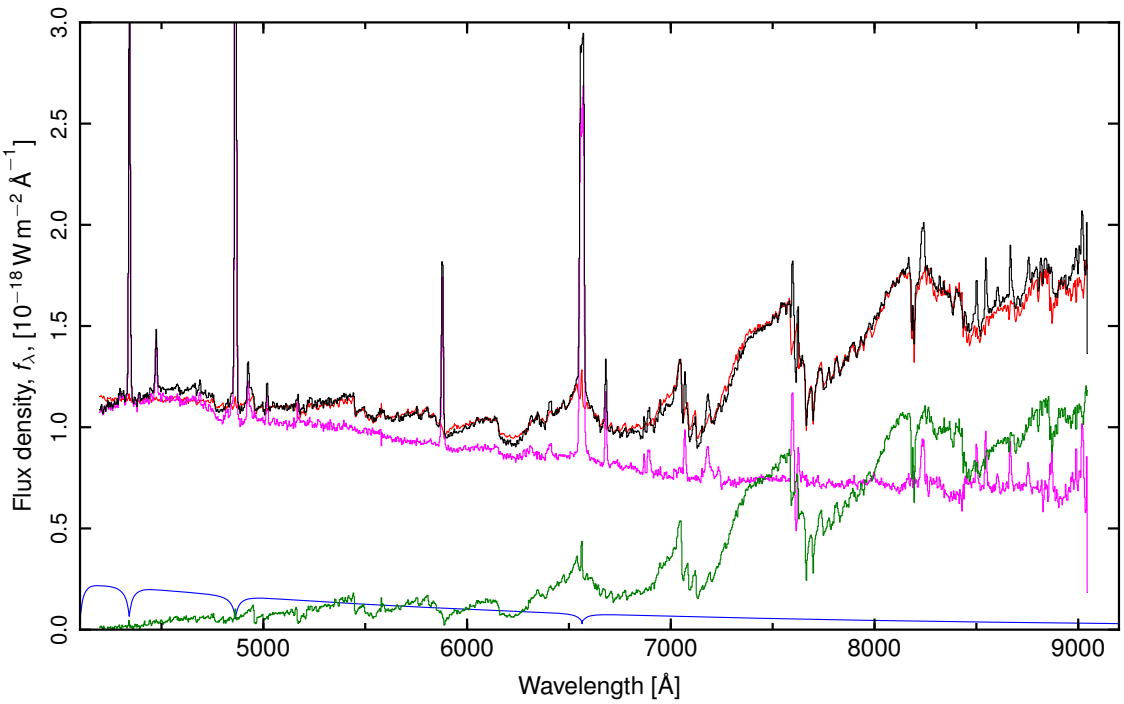

Extended Data Figure 1: The optical spectrum of the white dwarf's M star companion. A 10 minute exposure of AR Sco taken with FORS on the VLT between orbital phases 0.848 and 0.895 (black). Other spectra: an optimally-scaled M5 template (green); the sum of the template plus a fitted smooth spectrum (red); AR Sco minus the template, i.e. the extra light (magenta); a white dwarf model atmosphere of $T = 9750\,\mathrm{K}$, $\log g = 8.0$, the maximum possible consistent with the *HST* data (blue). A slit-loss factor of 0.61 has been applied to the models. The strong emission lines come from the irradiated face of the M star.

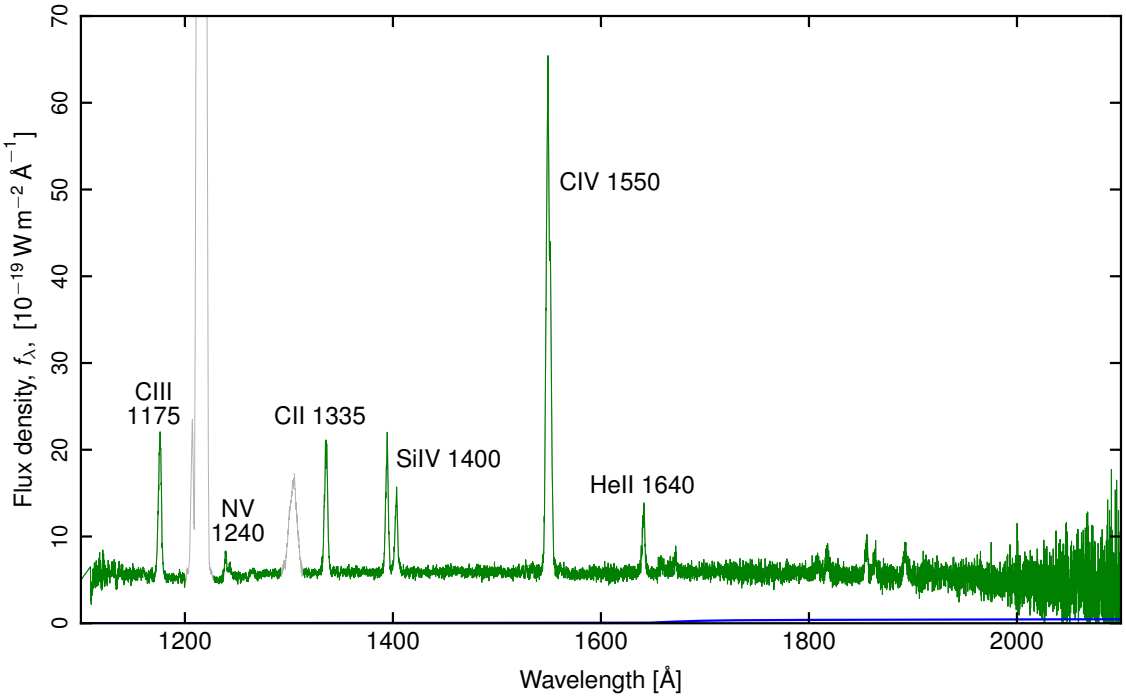

Extended Data Figure 2: *HST* ultraviolet spectrum of AR Sco. This shows the mean *HST* spectrum with geocoronal emission plotted in grey. The blue line close to the x-axis is a white dwarf model atmosphere of $T = 9750\,\mathrm{K}$, $\log g = 8.0$, representing the maximal contribution of the white dwarf consistent with light-curves. The radial velocities of the emission lines (Extended Data Fig. 4) show that, like the optical lines, the ultraviolet lines mainly come from the irradiated face of the M star.

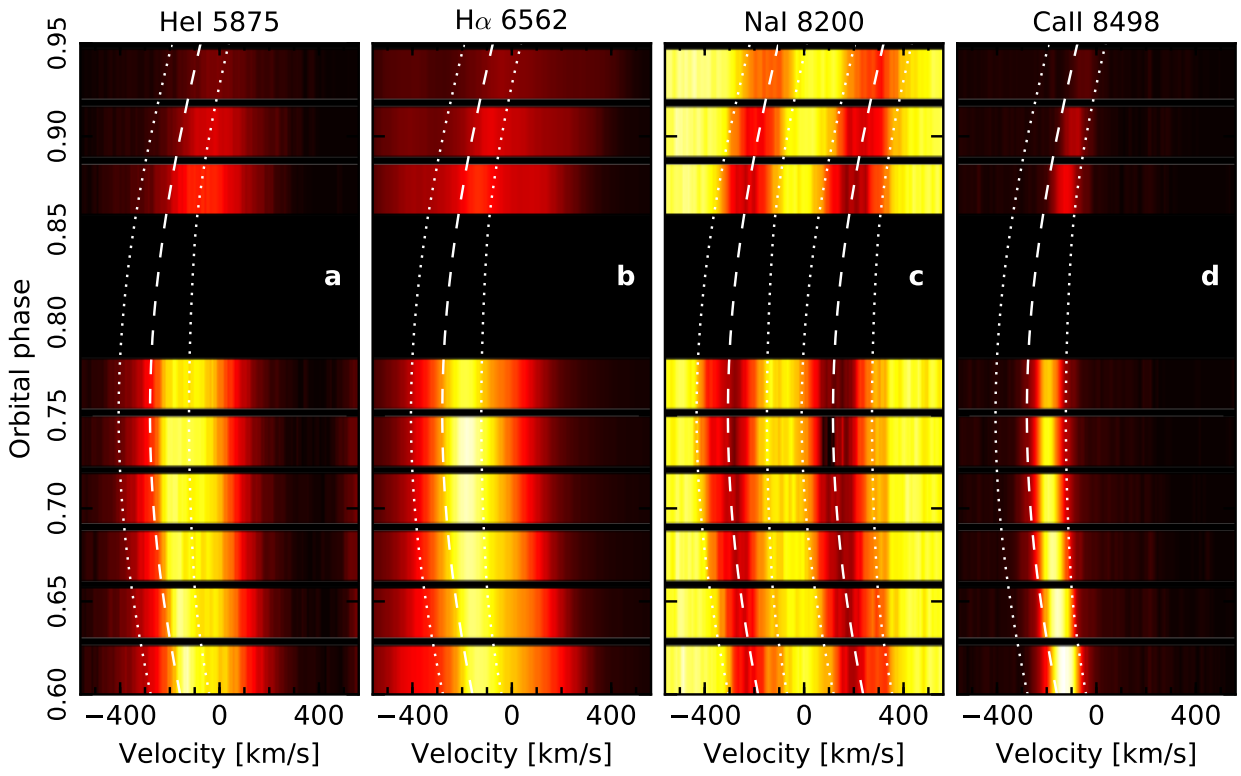

Extended Data Figure 3: Velocity variations of atomic emission lines compared to those of the M star. a, **b** and **d** show emission lines from a sequence of spectra from the VLT+X-SHOOTER data; **c** shows the NaI 8200 absorption doublet from the M star. The dashed line shows the motion of the centre of mass of the M star deduced from the NaI measurements while the dotted lines show the maximum range of radial velocities from the M star for $q = M_2/M_1 = 0.35$. The emission lines move in phase with the NaI doublet but at lower amplitude, showing that they come from the inner face of the M star.

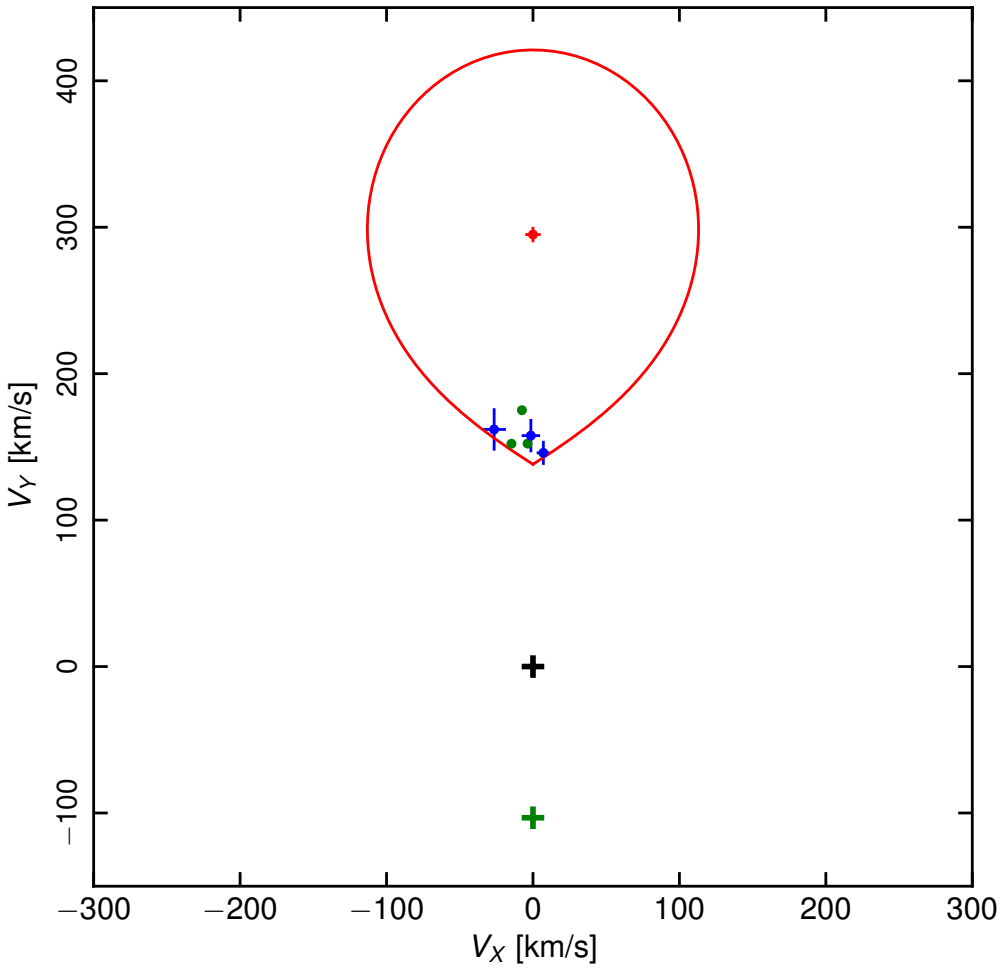

Extended Data Figure 4: The emission lines' origin relative to the M star. Velocities of the lines were fitted with $V_R = -V_X \cos 2\pi\phi + V_Y \sin 2\pi\phi$. The points show the values of (V_X, V_Y). Red: the M star from NaI (by definition this lies at $V_X = 0$). Blue: SiIV and HeII lines from the *HST* FUV data. Green: Hα, β and γ from optical spectroscopy. The black and green plus signs mark the centres of mass of the binary and white dwarf respectively. The red line shows the Roche lobe of the M star for a mass ratio $q = 0.35$.

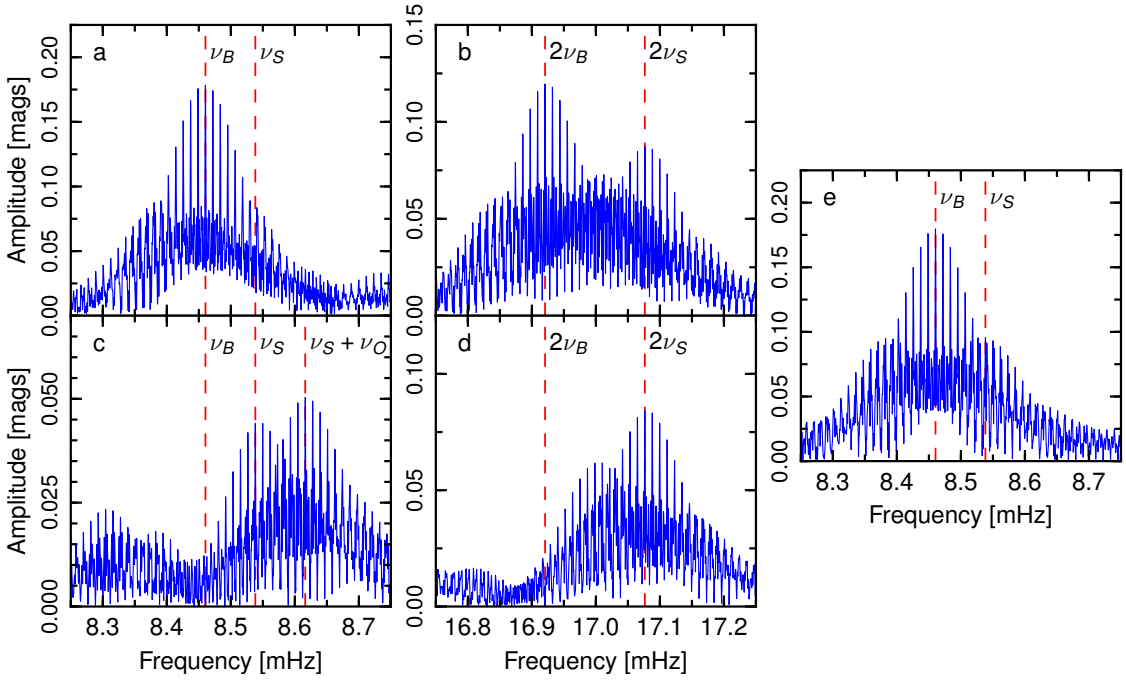

Extended Data Figure 5: Amplitude spectra from 9 days monitoring with a small telescope. **a**, Amplitude as a function of frequency around the $1.97\,\mathrm{min}$ signal from data taken with a $40\,\mathrm{cm}$ telescope. **b**, The same at the second harmonic. **c** and **d**, The same as **a** and **b** after subtracting the beat frequency signals at ν_B and $2\nu_\mathrm{B}$. Signals at $\nu_\mathrm{S} + \nu_\mathrm{O}$ and $2\nu_\mathrm{S} - \nu_\mathrm{O}$ are also apparent. **e**, The window function, computed from a pure sinusoid of frequency ν_B and amplitude 0.18 magnitudes (cf **a**).

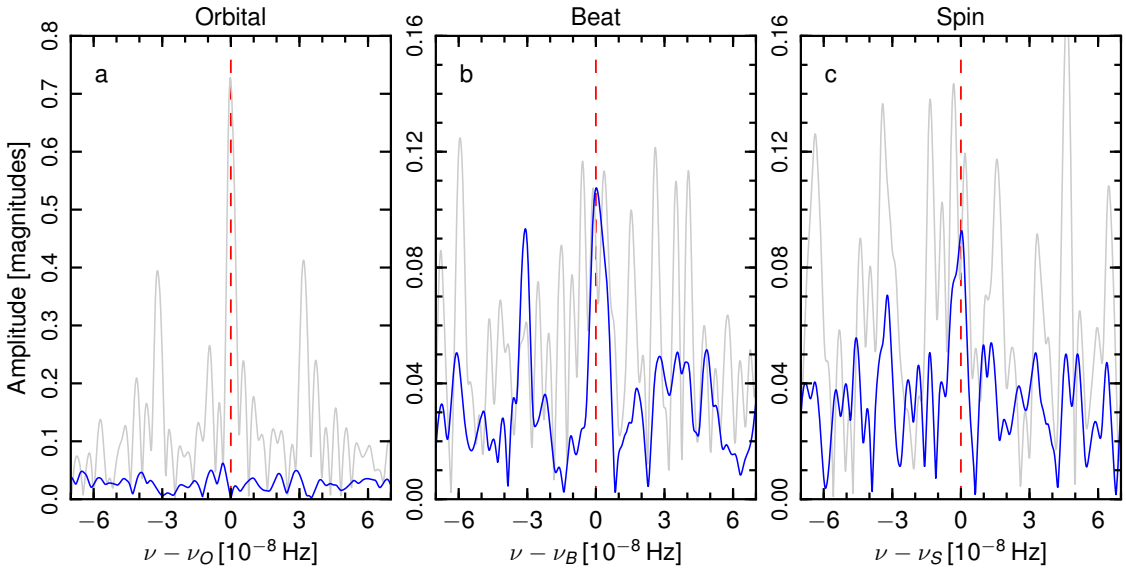

Extended Data Figure 6: Amplitude spectra from 7 years of sparsely-sampled CSS data. a-**c**, The amplitude as a function of frequency relative to the mean orbital (**a**), beat (**b**) and spin (**c**) frequencies listed in Extended Data Table 2. The grey line is the spectrum without any processing; the blue line is the spectrum after subtraction of the orbital signal.

Tel./Inst.	Type	Wavelength	Date	Exposure $T[\mathrm{s}] \times N$
VLT+FORS	Spectra	420 – 900 nm	2015-06-03	600x1
WHT+ULTRACAM	Photometry	u', g', r'	2015-06-23	2.9x768
WHT+ULTRACAM	Photometry	u', g', i'	2015-06-24	1.3x7634
Swift+UVOT/XRT	UV, X-rays	260 nm, 0.2 – 10 keV	2015-06-23 – 2015-08-03	1000x10
VLT+HAWKI	Photometry	K_S	2015-07-06	2.0x7020
WHT+ISIS	Spectra	354 – 539, 617 – 884 nm	2015-07-16	20x94
WHT+ISIS	Spectra	354 – 539, 617 – 884 nm	2015-07-17	300x4
WHT+ISIS	Spectra	356 – 520, 540 – 697 nm	2015-07-19	30x130
ROAD 40 cm	Photometry	White light	2015-07-19 – 2015-07-28	30x1932
WHT+ISIS	Spectra	356 – 520, 540 – 697 nm	2015-07-20	30x210
INT+IDS	Spectra	440 – 685 nm	2015-07-22	27x300
INT+IDS	Spectra	440 – 685 nm	2015-07-23	34x300
ATCA	Radio	5.5, 9.0 GHz	2015-08-13	271x10
WHT+ISIS	Spectra	320 – 535, 738 – 906 nm	2015-08-26	600x8
WHT+ISIS	Spectra	320 – 535, 738 – 906 nm	2015-09-01	600x8
VLT+XSHOOTER	Spectra	302 – 2479 nm	2015-09-23	11x300
HST+COS	Spectra	110 – 220 nm	2016-01-19	5 orbits
TNT+ULTRASPEC	Photometry	g'	2016-01-19	3.8x1061

Extended Data Table 1: Observation log.

Frequency	$5\,\%$-ile mHz	$95\,\%$-ile mHz	Median mHz	Mean mHz	RMS mHz
$\nu_{\rm O}$	0.077921311	0.077921449	0.077921380	0.077921380	0.000000042
$\nu_{\rm B}$	8.4603102	8.4603140	8.4603112	8.4603114	0.0000011
$\nu_{\rm S}$	8.5382332	8.5382356	8.5382348	8.5382346	0.0000008

Extended Data Table 2: Statistics of the orbital, beat and spin frequencies from bootstrap fits.

Source	Wavelength, Frequency	Flux mJy	Source	Wavelength, Frequency	Flux mJy
WISH	352 MHz	< 18	WISE	22.0 µm	45.2 – 105.4
FIRST	1.4 GHz	8.0 ± 0.3	WISE	12 µm	18.0 – 48.3
AT20G	20 GHz	< 50	*Spitzer*	5.73 µm	11.9 – 23.5
Herschel	500 µm	92 ± 25	WISE	4.60 µm	11.8 – 20.5
Herschel	350 µm	76 ± 21	*Spitzer*	3.6 µm	13.0 ± 0.7
Herschel	250 µm	55 ± 23	WISE	3.4 µm	13.2 – 13.8
Herschel	160 µm	118 ± 38	2MASS	2.1 µm	13.5 ± 0.3
Herschel	70 µm	196 ± 63	2MASS	1.7 µm	15.0 ± 0.3
Spitzer	24 µm	59.9 ± 6.0	2MASS	1.2 µm	13.3 ± 0.3

Extended Data Table 3: Archival data sources and flux values.